

Cite this: DOI: 10.1039/c0lc00362j

www.rsc.org/loc

PAPER

Programmed trapping of individual bacteria using micrometre-size sieves†

Min-Cheol Kim,^a Brett C. Isenberg,^a Jason Sutin,^b Amit Meller,^{ab} Joyce Y. Wong^a and Catherine M. Klapperich^{*a}

Received 31st August 2010, Accepted 6th January 2011

DOI: 10.1039/c0lc00362j

Monitoring the real-time behavior of spatial arrays of single living bacteria cells is only achieved with much experimental difficulty due to the small size and mobility of the cells. To address this problem, we have designed and constructed a simple microfluidic device capable of trapping single bacteria cells in spatially well-defined locations without the use of chemical surface treatments. The device exploits hydrodynamics to slow down and trap cells flowing near a narrow aperture. We have modeled this system numerically by approximating the motion of *Escherichia coli* cells as rigid 3-D ellipsoids. The numerical predictions for the speed and efficiency of trapping were tested by fabricating the devices and imaging GFP expressing *E. coli* at a high spatio-temporal resolution. We find that our numerical simulations agree well with the actual cell flow for varying trap geometries. The trapped cells are optically accessible, and combined with our ability to *predict* their spatial location we demonstrate the ease of this method for monitoring multiple single cells over a time course. The simplicity of the design, inexpensive materials and straightforward fabrication make it an accessible tool for any systems biology laboratory.

Introduction

The ability to monitor the molecular machinery of individual live cells over extended periods of time will open up new horizons in cell biology, as well as in emerging fields, including systems biology. When cells are individually monitored, their dynamical behavior *does not need to be synchronized*, and their individual responses are *not masked* by averaging over a bulk population of cells. These are powerful properties that drive the development of methods for live, individual cell probing. From an engineering perspective, an efficient, high-throughput, method for probing live cells depends on our ability to rationally design and fabricate devices in which cells are individually trapped, enabling prolonged high-resolution imaging. Since the trapping process itself can impact cell behavior, it is important that the trapping mechanism minimally affects the cells' phenotypic behavior, through either chemical or mechanical interactions. Here, we present a microfluidic platform suitable for high-resolution imaging of individually trapped bacteria that can be fabricated and operated in a simple manner and does not require special surface treatments to tether the trapped cells.

Much of the previous research requiring the isolation of single bacterial cells has been carried out in microtiter plates or

un-patterned microfluidic channels under very low flow speeds ($\sim 10 \mu\text{m s}^{-1}$), or in stationary conditions. Many labs use these techniques, but they can be very tedious, as it is extremely difficult to locate and/or track several different single cells when they are randomly located on a surface. As a result, it is easier to monitor one cell over a long period of time, an experimental practice that requires significant amounts of time to generate statistics.

Several groups have begun to develop microtechnologies to confine, address and monitor single cells. Most of these technologies were developed for mammalian cells.^{1–4} Confinement of single bacteria cells in wet etched silicon microwells has been recently reported.⁵ This method is limited, requires input of a very dilute bacteria solution and depends on sedimentation of the cells into the microwells in the absence of external flow controls. In other laboratories, analyses of individual bacteria have generally been performed by spreading cells on a glass cover slide coated with agarose gel.⁶ These methods are also hampered by the fact that very dilute solutions must be used to assure single cell resolution, and that finding a cell requires panning over an entire slide, making returning to a cell after looking at another on the same slide very difficult. It has been somewhat more common to “trap” adherent cells using soft lithography surface patterning, but most of these studies have been focused on changes in the attached cells as a function of the trapping geometry.^{7–9} For systems biology experiments, minimal impact of the trapping technology on the cell behavior is desired. Single cells have been trapped by several groups using droplet methods.¹⁰ Droplet based methods have great promise, but at this time they still require significant expertise to achieve.

^aDepartment of Biomedical Engineering, Boston University, 44 Cummings St., Boston, MA, 02215, USA. E-mail: catherin@bu.edu

^bDepartment of Physics, Boston University, Boston, MA, 02215, USA

† Electronic supplementary information (ESI) available: Details of ellipsoidal *E. coli* modeling and device fabrication. See DOI: 10.1039/c0lc00362j

To overcome these challenges, we demonstrate that hydrodynamic trapping is a highly predictable method to achieve inexpensive, high-throughput cell immobilization that is compatible with high-resolution optical imaging. Hydrodynamic trapping has been used successfully by many groups to trap comparatively large mammalian cells.^{11–14}

Here we describe the design of sieve-like cell traps (referred to as “sieves” hereafter) with openings just under one micron in size used to modify the flow field in a microfluidic cell in order to guide and arrest individual *Escherichia coli* cells in pre-defined locations. The ability of the sieves to trap cells was first evaluated in computer simulations that were then used to guide our device design. Trapping of individual cells in polydimethylsiloxane (PDMS)/glass devices was monitored by time-lapse fluorescence microscopy of GFP-labeled *E. coli* cells. Our results show remarkable agreement between the observed cell trajectories and the simulations.

Results

Flow modeling and *E. coli* cell simulation

Three different sieve types were used in simulations, and their abilities to trap cells were compared. All sieves were U-shaped positioned in a single specific pattern comprising eight identical sieves (numbered S1–S8), as shown in Fig. 1A. Three different sieve types were studied, where the entry angles, denoted: 0°, 15°

and 30°, were varied and the exit slit width was maintained at 0.8 μm (Fig. 1B). These variations in the apertures were used to determine the correlation between trapping performance and hydrodynamic resistance associated with the shape of the aperture.

Large differences in the fluid velocity distributions are observed in between sieves S7 and S8 and around S1 (Fig. 1C). However, we were mainly concerned with the fluid momentum *inside* the U-type sieves, as this determines the ability of the sieves to keep trapped cells in place once they enter. Noticeably, the simulated fluid velocity magnitude contours in all of the eight sieves were very low, less than 0.5 mm s^{−1} (Fig. 1C), suggesting that all sieves would be able to maintain trapped cells. For example, comparing this low fluid velocity with the diffusion-based velocity of *E. coli* ($\beta = 4$, see ESI† for more information), the diffusion velocities in the directions of \hat{x}_1 and \hat{x}_2 (Fig. S1†) can be calculated as 1.08 mm s^{−1} and 1.23 mm s^{−1}, respectively, using eqn (1) for a time step $\Delta t \approx 10^{-7}$ s,

$$V_{\text{diffusion}} = \sqrt{\frac{D_i}{2\Delta t}} \quad (1)$$

where D_i is the diffusion of the ellipsoidal particle in the direction of \hat{x}_i .¹³ This result implies that the diffusion based Brownian force dominates near the stagnation point, where the local fluid velocity is zero, and can act to throw the ellipsoidal bacteria from the trap. In addition, the calculated speed of the flow field at the aperture of each sieve was also very low.

Interestingly, by comparing the pattern of the contour lines near the stagnation point, for each sieve, with the streamlines passing through the aperture in each sieve, it can be inferred that the stagnation point is located along the corresponding streamline (Fig. 1C and D). The direction of the arrow in each sieve is almost identical to the normalized direction of gradient of the magnitude of the velocity ($\frac{\nabla|\vec{u}_t|}{|\nabla|\vec{u}_t||}$) where the slope (gradient) of the velocity magnitude contour lines is the least steep (Fig. 1B), and each sieve's stagnation point (Fig. 1D) is located at the intersection of the arrow in Fig. 1C and the stagnation plane (Fig. 1D), although the direction of the stagnation point flow is not parallel to the vertical line or flow direction at the inlet region. In particular, the streamlines are either tilted to the left (S3, S4, and S7) or to the right (S2, S6, and S8), or line up with the (S1 and S5) opening of each sieve (Fig. 1D), and directions are almost identical to the directions of the arrows in Fig. 1C. However, a streamline passing through any given aperture will match an ellipsoidal microbial cell's trajectory only if the cell is oriented parallel to the direction of the streamline, thus the probability of trapping a non-spherical cell will be smaller than the probability of trapping a spherical cell.

To investigate the dynamics of the ellipsoidal *E. coli* cell trapping process, cell loading in the individual trapping arrays for all three cases, 0°, 15° and 30°, was simulated at a prescribed flow rate (0.1 μl min^{−1}) and cell concentration (2 × 10⁷ CFU ml^{−1}). The detailed simulation method regarding the motion of ellipsoidal *E. coli* cell is described elsewhere.¹⁵ The variation of the trapped cell population in each sieve array was analyzed at discrete time points. Simulated temporo-spatial distributions of *E. coli* cells in one circular chamber for each sieve geometry were obtained every 10 s. Sample screen shots from each simulation

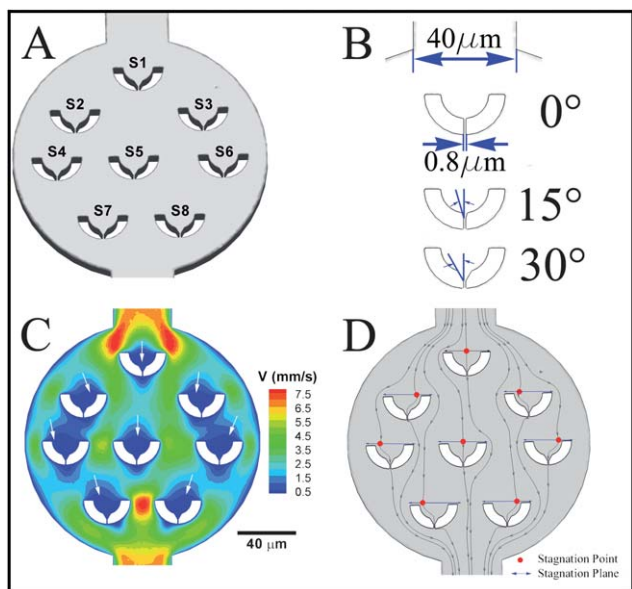


Fig. 1 Overview of the computational model. (A) Tilted view of the computational model of the trapping chamber; the chamber is circular with a diameter of 160 μm and a height of 10 μm, and each sieve is semicircular with an outer diameter of 30 μm, a height of 10 μm, and a width of 5 μm, and an 0.8 μm aperture. The numbers indicate each sieve by position. (B) Close-up drawing of each sieve design: 0°, 15° and 30°. (C) Contours of velocity magnitude in each sieve for an input flow rate of 0.1 μl min^{−1}; an arrow in each sieve represents the direction of the velocity gradient magnitude. (D) Selected streamlines passing through each sieve's aperture that pass through only one aperture each; the blue arrows and red point in each sieve indicate the stagnation plane and stagnation point, respectively.

are included in Fig. 2A–C, and images of actual trapped cells from experiments are shown in Fig. 2D and E. Temporal data are shown in Fig. S1 and S2†. The insets show sieve S2 for each case. An animation showing a detailed dynamic single cell trapping event is shown in Movie S1†.

Ellipsoidal *E. coli* cell motion

Due to its elongated shape, at flow rates higher than the swimming velocity, an *E. coli* cell in a laminar flow field will take on a different trajectory than a similarly sized spherical cell (Fig. 3A). The microbial cell was assumed to be a rigid ellipsoid with a major length of 4 μm and a minor length of 1 μm (Fig. 3B). An example of simulation data in Fig. 3C–E shows the continuous motion streams of a selected ellipsoidal cell continuous from the top and side views, the time-varying translational velocity components and the cell's orientation vector components. Here, the motion of the ellipsoidal cell in the microfluidic device was simulated using one-way coupled Lagrangian approach^{13,15} and rigid body dynamics based on the coordinate transformation (Fig. S3†) between the motion-frame system ($\hat{x}_1, \hat{x}_2, \hat{x}_3$) and the body-frame system ($\hat{x}_1, \hat{x}_2, \hat{x}_3$) in terms of Euler's four parameters (quaternion; $\varepsilon_1, \varepsilon_2, \varepsilon_3, \eta$)¹⁶ or the Euler angles (θ, ϕ , and ψ)¹⁷ (Fig. S1B†).

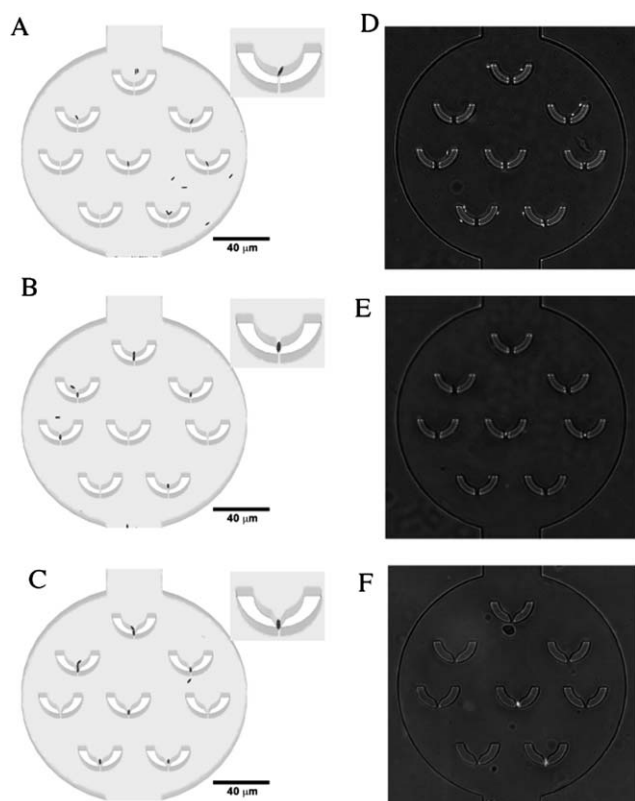


Fig. 2 Representative still images of experimental and simulation results. Simulation results for cell trapping based on an input cell density of 2×10^7 CFU ml^{-1} , a flow rate of $0.1 \mu\text{l min}^{-1}$ and a total physical time of 0.5 min, and comparative experimental cell trapping results using fluorescent K12 *E. coli*, with flow and cell density parameters matching those used in simulations; (A), (B), and (C) refer to the 0°, 15° and 30° aperture designs respectively.

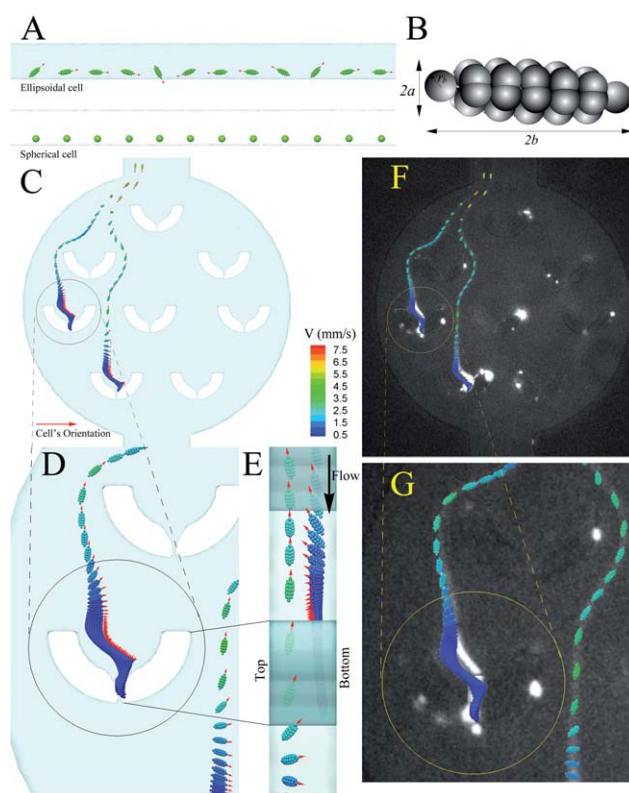


Fig. 3 Details of the computational model and selected results. (A) A comparison of the simulated trajectories of an ellipsoidal cell and a spherical cell in the same sized channel and same flow rate. (B) The ellipsoidal cell model constructed from 32 spheres. (C) Selected simulated trajectories of two ellipsoidal cells showing continuous motion streams with images at every 2 ms and (D) a magnified view of the circle marked in (C); the cell detours around the sieve at the volumetric flow rate of $0.1 \mu\text{l min}^{-1}$. (E) A side view showing how cell orientation varies throughout the flipping motion. (F) Superimposed images of the simulated data from (A) with the fluorescence trajectories of real *E. coli* cells in the fabricated device. (G) A magnified view of the circle marked in (G).

It should be noted that Fig. 3D and S2B† are related to Fig. 3E and S2C†, respectively; the flipping motion of one single ellipsoidal cell in the circle marked S4 (Fig. 3D) is shown in view of the yz plane (Fig. 3E). Longer distances between images of the cell indicate higher cell speed, and are observed at the entrance of the chamber (Fig. 3C–E). When the simulated cells were loaded into the microchamber, the initial orientation of each cell was set to the negative y -direction, parallel to the flow direction at the inlet. Before passing between S2 and S5, the cell moved to the tangential line of its center-connected trajectory, and the tumbling motion was observed at $t = 12$ ms. However, as the cell approached S7, it decelerated due to increased hydrodynamic resistance and stagnation flow near the sieve. The undisturbed region of the stagnation point was located on the horizontal line between two end tips of the U-type sieve as explained Fig. 1D. Detailed evolution of the cell orientation during its motion (Fig. 3C–E), and its orientations were found to be almost parallel to the stagnation plane. Deceleration near S7 was also observed during trapping experiments in fabricated devices (Fig. 3F and G). It was recorded as the brightest fluorescence intensity trajectory in a real device, where relatively bright intensity

represents low cell velocity, since a slow cell is in front of the camera longer than a fast cell. Images of simulated ellipsoidal *E. coli* cell's continuous motion streams (Fig. 3C and D) and fluorescence intensity trajectories were superimposed (Fig. 3F and G). The superpositions show agreement between the simulation and experiment. Both the simulation and validation experiments were carried out at a low volumetric flow rate of $0.1 \mu\text{L min}^{-1}$. Furthermore, our experimental results show that the ellipsoidal cell follows a similar trajectory as observed real cells (Movies S2–S5†, which if viewed in order show observed cells and modeled cells in similar locations in the chip).

Statistical analysis of device performance

We repeated the simulation ten times for each aperture case (0° , 15° and 30°) using different cell seeding profiles for the purpose of statistical analysis. For each simulation, the distribution of initial positions and chamber entrance times for each seeded cell were randomly generated using a uniform statistical distribution function (*Mathematica* 7.0, Wolfram Research, Champaign, IL) within the limitations of the inlet boundaries and total computational time.

The statistical distribution of trapped *E. coli* cells per sieve is illustrated in Fig. 4. Panels 4A and B show data from the simulations, 4C is a reconstruction of the same data taken during experiments. The error bars indicate the standard deviations obtained by counting the number of trapped cells for each case for each of the eight sieves. An ideal device would immobilize one and only one cell in every sieve. Since our devices are passively controlled, and trapping events are stochastically determined, we did not expect this to happen in our device. The simulations allowed us to predict, for a particular sieve aperture shape, what cell loading rate would result in the maximum number of single cell trapping events without overloading (more than one cell) the sieves. At a cell loading number of 333 CFU, the majority of sieves contain no cells (84%, 71%, and 69% for cases 0° , 15° and 30° , respectively). In all three cases, as more cells were loaded, there were noticeable decreases in the fraction of sieves containing zero cells: 69% (0°), 56% (15°), and 40% (30°) at 667 CFU and 58% (0°), 40% (15°), and 24% (30°) at 1000 CFU.

In addition to sieves with no trapped cells, there were also some sieves that trapped multiple cells in each case, since the trapping process follows Poisson statistics (Fig. 4A and B). Here, we establish a simple equation to convert the cell loading numbers into corresponding cell loading times on the condition that volumetric flow rate and cell concentration are known:

$$T_{\text{cell}} = \frac{N_{\text{cell}}}{\dot{m}_{\text{cell}}} = \frac{N_{\text{cell}}}{Q \times \rho_{\text{cell}}} \quad (2)$$

where T_{cell} represents “cell loading time [min]”, N_{cell} is “number of loaded cells [CFU]”, \dot{m}_{cell} is “cell loading rate [CFU min $^{-1}$]”, Q is “volumetric flow rate [ml min $^{-1}$]”, and ρ_{cell} is “cell concentration [CFU ml $^{-1}$]”.

We also analyzed the trapping performance of each sieve individually, and tried to find the correlation between trapping rates and volumetric flow rates in each of the eight sieves for all three cases 0° , 15° and 30° (Fig. S4†). The volumetric flow rate at each sieve was normalized to the flow rate at the inlet ($0.1 \mu\text{L min}^{-1}$). By comparing the ratios of the volumetric flow rates at

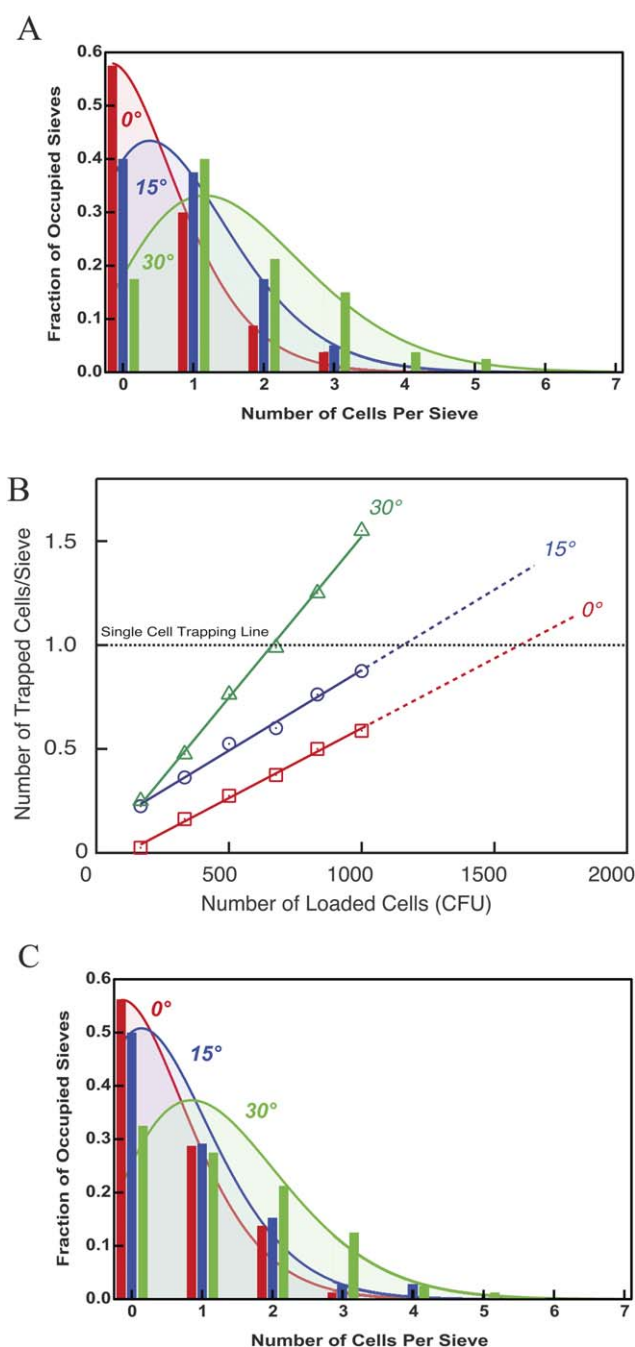


Fig. 4 Statistical analyses of simulation and experimental results. (A) Statistical analysis of the simulation results showing the distribution of cells per sieve as a function of the fraction of occupied sieves. Each curve represents a different sieve design, 0° , 15° and 30° . (B) Comparative simulated results for the number of trapped cells per a sieve vs. the number of loaded cells for the three different designs; the linear fits are $Y = -0.0721 + 6.71 \times 10^{-4} X$ (0°), $Y = -0.1059 + 7.73 \times 10^{-4} X$ (15°) and $Y = -0.0267 + 1.55 \times 10^{-3} X$ (30°) where X and Y correspond to the number of loaded cells (CFU) and the number of trapped cells per sieve, respectively. To trap, on average, a single cell per sieve ($Y = 1$), a loading amount of 1596 CFU is recommended for the case 0° , 1158 CFU for the case 15° and 662 CFU for the case 30° . (C) The identical analysis as in panel A was carried out for the experimental results acquired by counting cells trapped in each sieve using image analysis. Both plots indicate a Poisson distribution of trapped cells.

the inlet of S1 with that at the aperture of S1 in all three cases, the ratio for the 30° case is around 1.5 and is 2.0 times higher than those for cases 0° and 15°. This result implies that the design of the sieve in the 30° case leads to a lower hydrodynamic resistance around the sieve than in the other two cases. All three sieve designs showed same descending order of volumetric flow rates in the eight sieves: S1, S8, S7, S5, S4, S6, S3, and S2. Comparison of trapped cell populations in the eight sieves shows significantly higher values at sieve S1 in all cases. In addition, for case 0°, the number of trapped cells per sieve predicted by theory (0.59 ± 0.80 cells per sieve) is comparable to the 0.6 ± 0.77 obtained experimentally. For cases 15° and 30°, the theoretical *versus* experimental values are 0.88 ± 0.88 vs. 0.79 ± 0.99 and 1.41 ± 1.23 vs. 1.39 ± 1.40 cells per sieve, respectively. The higher standard deviation of the experimental results of cases 15° and 30° is not surprising, as cell-cell clumping is quite common, even in well-suspended cultures, leading to the deposition of small cell aggregates in the sieves.¹³

To demonstrate the predictive value of the model against an experimental platform, a comparison was made between the simulated cell loading of a U-shaped sieve array for each of the three designs 0°, 15° and 30° (with 0.8 µm wide apertures at their smallest point) and the experimental loading of PDMS microfluidic array devices with fluorescent K-12 *E. coli* cells (Fig. 2D–F)). Both simulations and experiments used a cell concentration of 2.0×10^7 CFU ml⁻¹, a bulk flow rate of 0.1 µl min⁻¹, and a total cell loading time of 30 s. The simulation results at a loading time of 30 s showed efficient capture of small cell populations in each sieve. Good agreement was shown between the simulation results and experimental cell trapping of fluorescent *E. coli* cells in the PDMS microfluidic device with respect to the number of individual sieves filled and the cell numbers per sieve. For the acquisition of experimental data, trapped cells in sieve arrays of 10 microchambers were counted using images taken using an inverted microscope for each case.

Using the simulated data, a plot of cell number per sieve as a function of the number of loaded cells ranging from 100 to 1000 CFU was constructed for all three designs, 0°, 15° and 30° (Fig. 4B). The number of trapped cells in a sieve is linearly related to the number of loaded cells, suggesting that the trapping rate (slope) is uniform. Previously, a simulation for trapping mammalian cells showed that the trapping rate was quadratic with respect to time for a period of ~15 s, after which very few cells are deposited in the traps for extended loading periods.¹³ Thus, when a large enough number of cells are trapped, the trapping rate with respect to the number of loaded cells is saturated. For *E. coli* cells, which are much smaller than mammalian cells, the time for saturation will be longer than for mammalian cells because the sieves have a larger capacity for trapping *E. coli* cells. These linear curves are useful for the determination of the time needed to trap one and only one cell per sieve before the onset of multiple trapping per sieve. The number of loaded cells can be converted to loading time by applying eqn (2).

Application of the single cell trapping device

To demonstrate the potential of the device in a systems biology application, we performed the following experiment. In time-

lapse experiments, fluorescence was monitored from genetically encoded RNA sensors expressed in live MB45 cells. MB45 is a previously described strain of BL21(DE3) *E. coli* in which fluorescence occurs upon the formation of a binary protein complex on a 58 ribonucleotide aptamer tag encoded in a specific target RNA sequence.¹⁸ The binary complex consists of two-fusion proteins, each containing a portion of the eGFP protein and a portion of the eukaryotic initiation factor 4A (eIF4A). Alone, each eGFP fragment is insufficient to generate fluorescence. However, binding of eIF4A portions of the fragments to the aptamer sequence drives protein complementation of the eGFP fragments, generating a functional fluorophore. Thus, the fluorescence intensity indicates the local concentration of the target RNA molecules within the cell.¹⁹ Cells were grown and expression was induced by IPTG as previously described¹⁸ and then transferred to PBS for imaging.¹⁹ Fig. 5A shows a representative image of one such trapped *E. coli* in a device with the 30° sieve design. We tracked a single cell's fluorescence over an 18 min time course; images were taken of the cell trapped in the bottom right sieve (S8) at 2 min intervals (Fig. 5B).

Discussion

The simulations and experiments presented here allow for the fabrication and assembly of very simple cell trapping devices capable of creating arrays of single cells that are observable using light microscopy. The main features of our method are: (1) the trapped cells are minimally impacted due to the pure hydrodynamic mechanism employed; (2) continuous perfusion of trapped cells during experiments is enabled; (3) the observed relationships between the cell loading parameters and cell trapping behavior determined by simulation and experiment can be used to predict the trapping ability of the setup.

For example, for a particular loading time, if the loading rate is known, the cell seeding time can be adjusted to achieve the optimal seeding density. Ideally, one wants one cell per sieve and no more or no less than one cell. By controlling the seeding conditions, one can closely approach these ideal conditions. Specifically, using a cell loading rate of 2000 CFU min⁻¹ and the linear fits in Fig. 4B are $Y = -0.0721 + 6.71 \times 10^{-4} X$ (case 0°), $Y = -0.1059 + 7.73 \times 10^{-4} X$ (case 15°) and $Y = -0.0267 + 1.55 \times 10^{-3} X$ (case 30°) where X and Y are the number of loaded cells (CFU) and the number of trapped cells per a sieve respectively. Total cell loadings of 1596 CFU for the case 0°, 1158 CFU for the case 15° and 662 CFU for the case 30° are recommended to trap a single cell per a sieve ($Y = 1$). Thus, the corresponding cell loading times leading to the greatest number of filled sieves with the least number of sieves with more than one trapped cell for the three cases, 0°, 15° and 30° are approximated as 48 s, 35 s, and 20 s, respectively.

There are some notable limitations to our technique. The simulations were carried out using a single circular chamber, while the experiments were carried out a larger device comprising 10 circular chambers. As a result, the loading time in the simulation was limited to a single chamber. That is to say, the cell loading time in the experiment is longer than in the simulation due to the longer entrance channel to the circular chamber and the larger number of chambers. Further, due to the low probability for one and only one cell trapping, this method is not

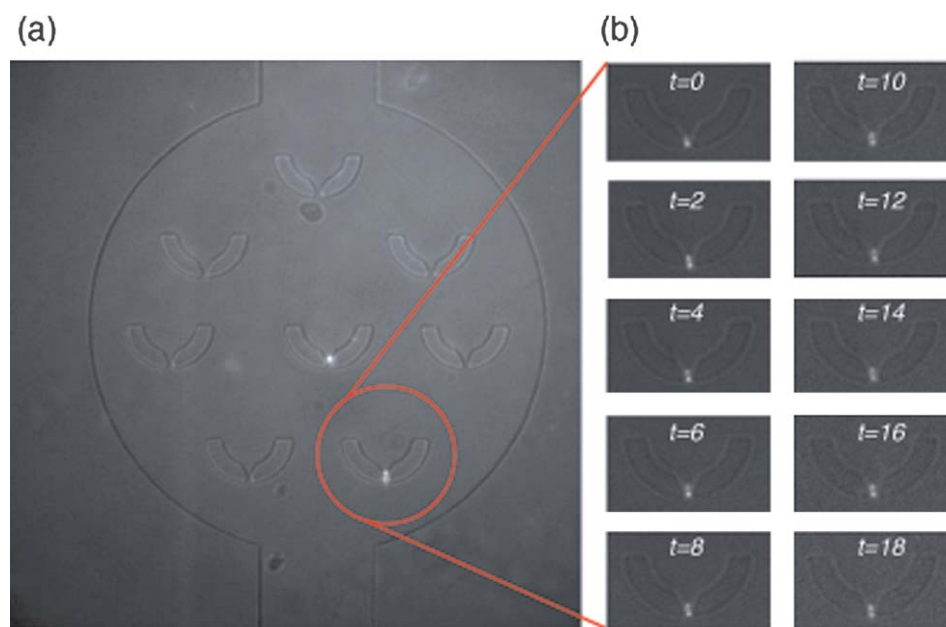


Fig. 5 Demonstration of imaging a living cell trapped in a device over a time course. (A) Image of trapped *E. coli* in a device with the 30° sieve design. (B) Time course fluorescence images taken every two minutes of the cell trapped in the bottom right sieve, demonstrating the ability to track a single cell over an 18 minute time course.

suitable for very low input concentrations of bacteria, which would require very long cell loading times. The third case, case 30°, showed the highest trapping rate of 10 cells trapped per 1000 cells loaded (1%). In general, this will not be a problem, since most bacterial cultures provide significantly larger populations in relatively short amounts of time. This method is also not suitable for very high flow rate loadings. Increasing flow rate significantly may lead to lysis of the trapped bacteria. This feature may be used, however, to lyse a small population of cells after an experiment is finished for further analysis. If one wanted to remove cells for analysis without lysis, a simply reversing the direction of flow should be sufficient.

The numerical studies presented here simulating individual bacterium motion apply Lagrangian methods and rigid body dynamics to the design of a microfluidic device to trap single bacterium in specific locations. Our computational model is different from the computational swimming models^{20,21} in several respects (see ESI†, Discussion). Particles that entered the device parallel to the direction of flow all exhibited similar orientations as they flowed through the device. However, the trajectory of an ellipsoidal particle is strongly dependent on its initial orientation as it enters vortices;²² for instance, when an ellipsoidal particle enters a stagnation flow region and its initial orientation is 45° from the flow direction, it moves further away from the stagnation point (center) than a cell whose initial orientation as parallel to the principal directions of the flow field (see ESI†, Movies). This observation may facilitate a better understanding of the ellipsoidal cell trapping conditions.

Most importantly, the cell trapping device described here is suitable for use in any research lab with access to simple microfabrication techniques. Since many devices can be made from a single mold, the microfabrication work can be done outside of the lab for time and cost savings. No special surface

treatments are necessary to hold the bacteria in place, and a simple syringe pump and fittings are suitable for running experiments.

In conclusion, a novel simulation method to model the trapping of ellipsoidal *E. coli* cells in sieve structures within a microfluidic device has been improved by considering rigid body motion (translation and rotation) with a one-way coupling approach between the particle motion and the surrounding flow field. In addition, a novel model of an ellipsoidal cell made up of thirty-two connected beads was constructed to model the interactions between the cell surface and the solid wall boundaries of the PDMS microfluidic device. As a result, using this simulation method, the most efficient of three designs for the trapping of one single cell per sieve was readily acquired by counting the number of trapped cells at the individual sieve after specific cell loading times. We found two interesting phenomena in this single cell trapping microfluidic device; first, the probability of immobilizing cells in a sieve decreases as you decrease the aperture size, enabling single cell trapping of *E. coli* even with a high cell density loading ($\sim 10^7$ CFU ml⁻¹). Second, the stagnation point flows near the sieve appear to enhance trapping. In addition, the developed simulation method is modifiable and could be further applied to solve for the motion of any axially symmetrical cells while considering elastic deformation of the cell.

Methods

Design based fluid modeling

A user-specified computational model of the microfluidic system was built (Fig. S4†). First, 2-D CAD drawings of the proposed systems were drawn and extruded into 3-D solid models using AutoCAD software (Autodesk, Inc, San Rafael, CA). The STL

(stereolithography) file format was used and the objects were extruded in the direction of the channel height. Second, the surface geometry of STL file was imported into auto-meshing software (PRO-AM, CD-adapco, London, UK),²³ and computational cell shapes were optimized (Fig. S4†, left panel). In particular, the selection of minimum and maximum lengths for surface triangulation in the trapping sieves was based on the sieve aperture size (Fig. S4†, right panel). Once the surface mesh was optimized, the subsurface was generated, which involved shrinking the original model in all areas except the inlet and outlet regions. Extrusion layers were made from the subsurface. Extrusion layers are useful for computations of cell rolling in the near-wall region, *i.e.* for interactions between cells and the inner surface of microchannel. Finally, the 3-D computational model was completed by joining the two types of mesh at the inner domain of the tetrahedron and extrusion layers of the triangular prism.^{13,23}

Computational fluid dynamics (CFD) simulations were carried out using the commercial CFD tool STAR-CD version 4.06 (CD-adapco, London, UK),²⁴ which is based on finite volume method (FVM). An aqueous solution was selected to transfer cells into patterned micro-chambers. The momentum equations and the continuity equation were solved using the SIMPLE (Semi-Implicit Method for Pressure Linked Equation) algorithm²⁵ with a tolerance of 1.0×10^{-6} . The SIMPLE algorithm was used for the calculation of steady problems with one predictor stage and one corrector stage iteratively. The algebraic multigrid (AMG) approach was used as the linear solver, since it is independent of geometry.²⁴ For the numerical scheme, UD (upwind scheme; 1st order of accuracy) for the spatial discretization was used with residual tolerances of 0.1 for each velocity component and 0.05 for pressure. An aqueous solution containing ellipsoidal cells was supplied with a flat velocity profile and a uniform flow rate of $0.1 \mu\text{l min}^{-1}$ at the inlet boundary. At the outlet, a pressure boundary condition was imposed.

E. coli trapping experiments

Stainless steel connectors (New England Small Tube Corp., Litchfield, NH) were inserted into the ports of the devices and linked to 3 cm³ syringes (Becton Dickinson, Franklin Lakes, New Jersey) by Tygon microbore tubing (Cole Parmer, Vernon Hills, IL). Images of the photolithographic masks and device molds are included in Fig. S5†. The devices were first primed by flushing the channels with PBS followed by the injection of PBS containing *E. coli* at a concentration of 2×10^7 CFU ml⁻¹ at a flow rate of 0.1 ml min^{-1} through each trap using a syringe pump (Harvard Apparatus, Holliston, MA). *E. coli* trapping events were imaged

using a Zeiss 40× 1.1 NA water immersion microscope objective in a Zeiss Axiovert 100M inverted microscope. Images at higher magnifications were obtained using an optional 1.6× magnification tube lens. A beam from a 488 nm laser (Coherent, Santa Clara, CA) was expanded through the objective to epi-illuminate the device over the field of view of the camera. Fluorescence emission from the bacteria was collected through a 525/50 nm bandpass filter (Semrock, Rochester, NY) and detected with an iXon EMCCD camera (Andor, South Windsor, CT).

References

- 1 A. M. Skelley, O. Kirak, H. Suh, R. Jaenisch and J. Voldman, *Nat. Methods*, 2009, **6**, 147–152.
- 2 Y. Gao, S. Bhattacharya, X. Chen, S. Barizuddin, S. Gangopadhyay and K. D. Gillis, *Lab Chip*, 2009, **9**, 3442–3446.
- 3 S. Kobel, A. Valero, J. Latt, P. Renaud and M. Lutolf, *Lab Chip*, 2010, **10**, 857–863.
- 4 J. Nilsson, M. Evander, B. Hammarstrom and T. Laurell, *Anal. Chim. Acta*, 2009, **649**, 141–157.
- 5 I. Choi, Y. I. Yang, Y. J. Kim, Y. Kim, J. S. Hahn, K. Choi and J. Yi, *Langmuir*, 2008, **24**, 2597–2602.
- 6 J. F. Jones and D. Velegol, *Colloids Surf., B*, 2006, **50**, 66–71.
- 7 S. Park, P. M. Wolanin, E. A. Yuzbashyan, H. Lin, N. C. Darnton, J. B. Stock, P. Silberzan and R. Austin, *Proc. Natl. Acad. Sci. U. S. A.*, 2003, **100**, 13910–13915.
- 8 C. S. Chen, M. Mrksich, S. Huang, G. M. Whitesides and D. E. Ingber, *Science*, 1997, **276**, 1425–1428.
- 9 C. S. Chen, M. Mrksich, S. Huang, G. M. Whitesides and D. E. Ingber, *Biotechnol. Prog.*, 1998, **14**, 356–363.
- 10 J. Q. Boedicker, M. E. Vincent and R. F. Ismagilov, *Angew. Chem., Int. Ed.*, 2009, **48**, 5908–5911.
- 11 D. Di Carlo, N. Aghdam and L. P. Lee, *Anal. Chem.*, 2006, **78**, 4925–4930.
- 12 D. Di Carlo, L. Y. Wu and L. P. Lee, *Lab Chip*, 2006, **6**, 1445–1449.
- 13 M. C. Kim, Z. H. Wang, R. H. W. Lam and T. Thorsen, *J. Appl. Phys.*, 2008, **103**, 044701.
- 14 P. C. Li, L. de Camprieux, J. Cai and M. Sangar, *Lab Chip*, 2004, **4**, 174–180.
- 15 M. C. Kim and C. M. Klapperich, *Lab Chip*, 2010, **10**, 2464–2471.
- 16 H. Goldstein, *Classical Mechanics*, Addison-Wesley Pub. Co., Reading, MA, 1980.
- 17 P. C. Hughes, *Spacecraft Attitude Dynamics*, J. Wiley, New York, 1986.
- 18 M. Valencia-Burton, R. M. McCullough, C. R. Cantor and N. E. Broude, *Nat. Methods*, 2007, **4**, 421–427.
- 19 M. Valencia-Burton, A. Shah, J. Sutin, A. Borogovac, R. M. McCullough, C. R. Cantor, A. Meller and N. E. Broude, *Proc. Natl. Acad. Sci. U. S. A.*, 2009, **106**, 16399–16404.
- 20 M. Ramia, D. L. Tullock and N. Phan-Thien, *Biophys. J.*, 1993, **65**, 755–778.
- 21 T. Goto, K. Nakata, K. Baba, M. Nishimura and Y. Magariyama, *Biophys. J.*, 2005, **89**, 3771–3779.
- 22 F. G. Fan and G. Ahmadi, *J. Aerosol Sci.*, 1995, **26**, 813–840.
- 23 CD-adapco, 2007.
- 24 *Methodology*, CD-adapco, 2007.
- 25 S. V. Patankar, *Numerical Heat Transfer and Fluid Flow*, Hemisphere Pub. Corp.; McGraw-Hill, Washington, New York, 1980.